water

MDPI

Article

Insight from a Physical-Based Model for the Triggering Mechanism of Loess Landslides Induced by the 2013 Tianshui Heavy Rainfall Event

Siyuan Ma [1,2], Xiaoyi Shao [3,4], Chong Xu [3,4,*] and Yueren Xu [5]

[1] Institute of Geology, China Earthquake Administration, Beijing 100029, China
[2] Key Laboratory of Seismic and Volcanic Hazards, Institute of Geology, China Earthquake Administration, Beijing 100029, China
[3] National Institute of Natural Hazards, Ministry of Emergency Management of China, Beijing 100085, China
[4] Key Laboratory of Compound and Chained Natural Hazards Dynamics, Ministry of Emergency Management of China, Beijing 100085, China
[5] Key Laboratory of Earthquake Prediction, Institute of Earthquake Forecasting, China Earthquake Administration, Beijing 100036, China
* Correspondence: xc11111111@126.com or chongxu@ninhm.ac.cn

Abstract: Rainfall-induced landslides pose a significant threat to human life, destroy highways and railways, and cause farmland degradation in the Loess Plateau. From 19 June 2013 to 26 July 2013, continuous and heavy rainfall events occurred in the Tianshui area, Gansu Province. This strong rainfall process included four short-term serious rainfall events and long-term intermittent rainfall, triggering many shallow loess landslides. To improve our understanding of this rainfall process as the triggering mechanism of the loess landslides, we conducted the physical-based spatiotemporal prediction of rainfall-induced landslides. By utilizing precipitation data recorded every 12 h from the rain gauge stations and 51 soil samples from within a 50 km radius of the study area, we predicted 1000 physical-based model-calculated pictures of potential landslides, and the slope failure probability (Pf) of the study area was obtained by Monte Carlo simulations. The model was validated by the actual landslide data of the 2013 heavy rainfall event, and the effects of the precipitation process and the trigger mechanism on the landslides were discussed. The results showed that the fourth rainfall event had the best prediction ability, while the third event had the second-best prediction ability. There was a solid linear link between the antecedent precipitation (P_a) and the predicted landslide area (P_{ls}) based on the fitting relationship, indicating that antecedent rainfall may play a significant role in the occurrence of landslides in the region. By comparing the distribution of the predicted results of the four heavy rainfall events with the actual landslide, we observed that the first two rainfall processes may not have been the main reason for slope failure, contributing only to prepare for the landslides in the later period. The superposition of the fourth and third rainfall events finally determined the spatial distribution characteristics of the landslide induced by the 2013 heavy rainfall event.

Keywords: heavy rainfall; loess landslide; physical-based model; FSLAM model; triggering mechanism; hazard assessment; Tianshui area; Gansu Province

Citation: Ma, S.; Shao, X.; Xu, C.; Xu, Y. Insight from a Physical-Based Model for the Triggering Mechanism of Loess Landslides Induced by the 2013 Tianshui Heavy Rainfall Event. *Water* **2023**, *15*, 443. https://doi.org/10.3390/w15030443

Academic Editors: Zizheng Guo, Samuele Segoni and Yixiang Song

Received: 3 January 2023
Revised: 18 January 2023
Accepted: 18 January 2023
Published: 22 January 2023

1. Introduction

Due to the influence of global extreme climate change, there have been more extreme rainfall events in mountain areas in recent years, dramatically increasing the frequency of rainfall-induced landslides globally [1,2]. Compared with other natural hazards such as volcanic eruptions and floods, rainfall-induced landslides cause significant human harm as well as substantial economic losses [3–6].

Many studies have adopted a variety of methods to carry out the spatiotemporal prediction of rainfall-induced landslides [7], which mainly include an empirical method, a data-driven method, and a physical-based method. The empirical method is based on historical landslide data and rainfall records to analyze the relationship between rainfall characteristics and landslide occurrence [8–10]. The process is simple and easy to use, but it only considers rainfall and ignores other geological and hydrological conditions. As a result, this method is only applicable in areas with similar geological and geomorphic characteristics [11–13]. Furthermore, the empirical method requires abundant landslide and rainfall data, so it fails to develop an effective rainfall threshold in mountain areas where landslide and rainfall data are scarce. The data-driven method uses mathematical models to examine the relationships between influencing factors and landslide occurrence [14–16]. The landslide hazard assessment of the study area can be carried out using known models. However, because data-driven models are trained using regional landslide data and, thus, limited by the area's geological and geomorphic characteristics, the data-driven method still has regional constraints in the spatial prediction of rainfall-induced landslides.

The physical-based method, in contrast to the data-driven method, does not use actual landslide data, but rather simulates the physical process of rainfall-induced landslide occurrence by combining hydrological and infinite slope models [17]. Because of their preferable practicability and wide regional applicability, physical-based models have been widely used in the spatial prediction of regional rainfall-induced landslides. The establishment of hydrological models is the most difficult issue in physical-based rainfall landslide hazard assessment. The most commonly used hydrological models include the steady-state model and the transient-state model [18]. The steady-state model assumes a stable rainfall infiltration process and saturated water retention parallel to the slope surface. As a result, the model assumes that the changes in groundwater flow and long-term rainfall affect the uniform recharge state of the groundwater rather than being caused by a single rainfall event. The popular models include the SHALSTAB [19,20] and SINMAP models [21]. Although the steady-state hydrological model is useful for assessing slope stability over a large area, the model is limited to a few unrealistic situations related to rainfall characteristics and site conditions, and it lacks prediction for real rainfall scenarios [17].

In recent years, some physical-based models based on the transient-state hydrological model have been developed, such as the SLIP model [22–24], GIS-TiVaSS model [25,26], GIS-TISSA model [27], CRESTSLIDE model [28,29], HIRESSS model [30–32], and TRIGRS model [17], which have been widely used in the spatiotemporal prediction and early warning of rainfall-induced landslides. However, one of the challenges in applying the transient-state hydrological model is the requirement for a large amount of input data, such as mechanical and hydrological parameters of the study area [33–36]. Meanwhile, these transient-state hydrological models only consider the impact of vertical seepage from short-term heavy rainfall events on groundwater levels, ignoring the effect of lateral flow on long-term groundwater levels in mid–long-term precipitation, resulting in underestimation of the assessment results.

Furthermore, most previous works do not take the uncertainty of the input data into account, instead using the deterministic analytical method to calculate the probability of slope failure. However, because the deterministic analysis method ignores spatial heterogeneity and uncertainty of the soil data, providing only a single fixed value for the uncertainty of the input parameters is inappropriate [12,37–41]. Especially at a large scale, there are certain difficulties in obtaining a large number of input data, resulting in possible errors in the quality of the input data and unsatisfactory prediction results [11]. This spatial uncertainty and heterogeneity analysis can consider the probability, so it is regarded as an effective method for dealing with data uncertainty and heterogeneity [12,38,39,42–45].

Given the current issues with the physical-based models, Medina et al. [46] developed a new physical-based model called "Fast Shallow Landslide Assessment Model" (FSLAM) that can be used for large areas (>100 km^2) with a high-resolution topography in a very short computational time. Meanwhile, this model can consider the combined effects of

the lateral and vertical flows to calculate the water table and the uncertainty of the input parameters well, showing great potential in the spatiotemporal landslide prediction of large areas [46,47]. The 2013 heavy rainfall event was the longest and most serious rainfall since the meteorological records in the Tianshui area began, resulting in 50,000 individuals affected and 24 deaths, nearly 10,000 houses destroyed, and a direct economic loss of RMB 8.4 billion. This rainfall event induced about 54,000 shallow landslides and debris flows in the Tianshui area [48], providing us with an invaluable window to investigate the distribution patterns and triggering mechanisms of rainfall-induced landslides in this area. Although Qi et al. [49] utilized machine learning to map the landslide susceptibility in this area, there has been no study on the spatiotemporal prediction of rainfall-induced landslides from this rainfall event using a physical-based model—especially for the FSLAM model, which has not been applied in the Loess Plateau region. Meanwhile, the analysis of rainfall processes and triggering mechanisms for landslide occurrence from this event is still very limited. To improve our understanding of the effects of this rainfall process on the triggering mechanisms of the loess landslides, we conducted the physical-based spatiotemporal prediction of rainfall-induced landslides based on the FSLAM model. The model was validated by applying the actual shallow landslide data from the 2013 rainfall event. Finally, the effects of precipitation parameters and trigger mechanisms on shallow landslides are discussed.

2. Study Area

2.1. General Settings

The study area is located in a basin (34.3° N~34.8° N and 106.0° E~106.3° E) near the Maiji area of Tianshui, Gansu Province, with an area of about 520 km^2. The study area has a loess hilly landform formed by Quaternary loess deposits, with an elevation range of 900–2100 m (Figure 1). The climate in the region is warm, temperate, and semi-humid, with an average temperature of 11.5 °C. The minimum temperature is −18 °C, and the maximum temperature is 35 °C. The annual rainfall in the study area is 500 mm, and most of the rainfall is concentrated in June, July, and August. Among these months, the rainfall in July is the greatest, with a monthly average rainfall of about 100 mm. In 2013, the monthly rainfall reached twice the average rainfall (Figure 2).

The study area's strata include Quaternary sediments (Q3 and Q4), Tertiary sedimentary rocks (N and E), Devonian clastic rocks (D2s), and magmatic rocks (Mag). Quaternary sediments are the most widely distributed strata, accounting for about 50% of the total area. The Quaternary sediments are primarily Late Quaternary loess (Q3eol), with a small number of fluvial deposits (Q4a-pl) distributed along both sides of the rivers. The Tertiary sedimentary rocks include gray–white clay rock and red mudstone of the Neogene (N) and conglomerate, purplish–red glutenite of the Paleogene (E). The Devonian clastic rocks (D2s) are mainly argillaceous slate and quartz sandstone of the Shujiaba formation, accounting for less 10% of the total area (Figure 3). Furthermore, the study area contains dense forest and cropland, but there are also dense residential areas and roads in the east of the area, including the towns of Shetang and Mabaoquan, with significant population growth and urbanization (Figure 4).

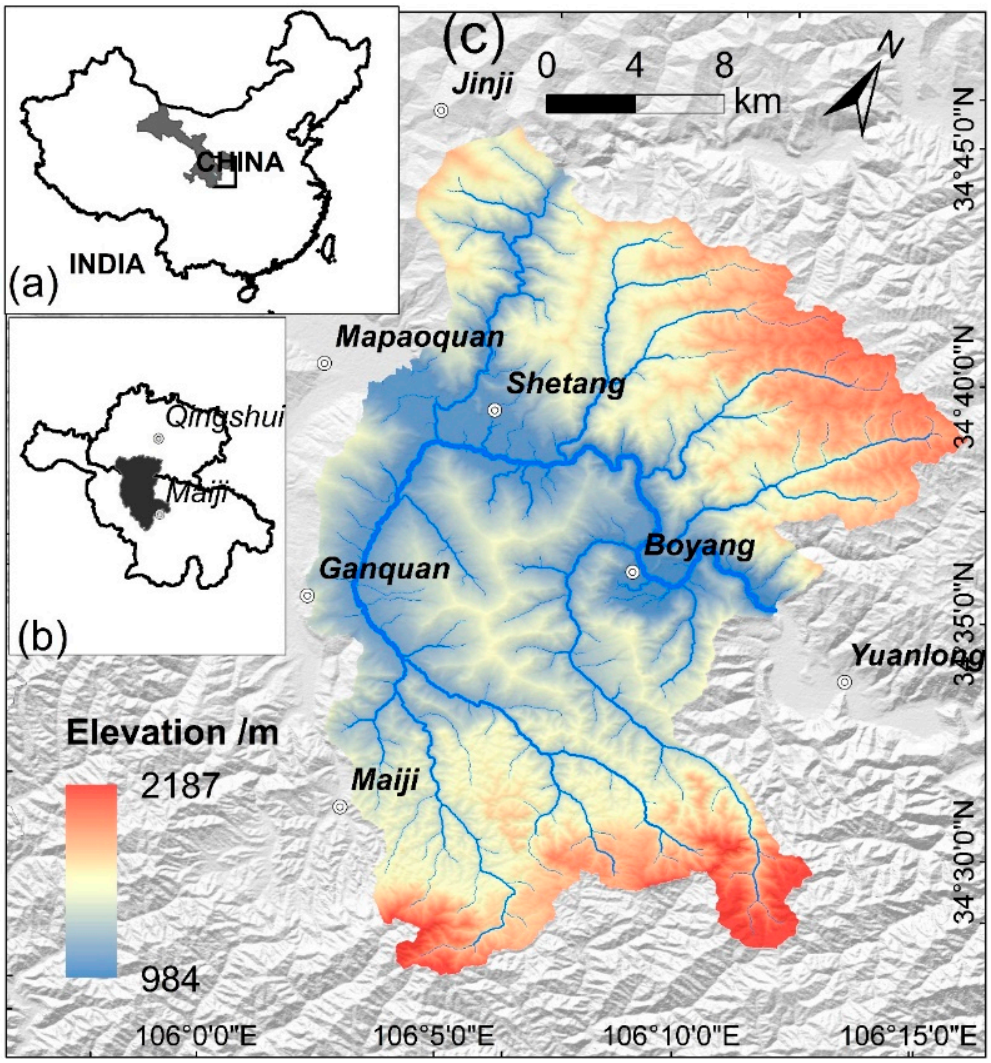

Figure 1. Map showing the location of the study area and its topography: (**a**) Gansu Province. (**b**) The location of Tianshui. (**c**) The distribution of elevation and the main rivers in the study area.

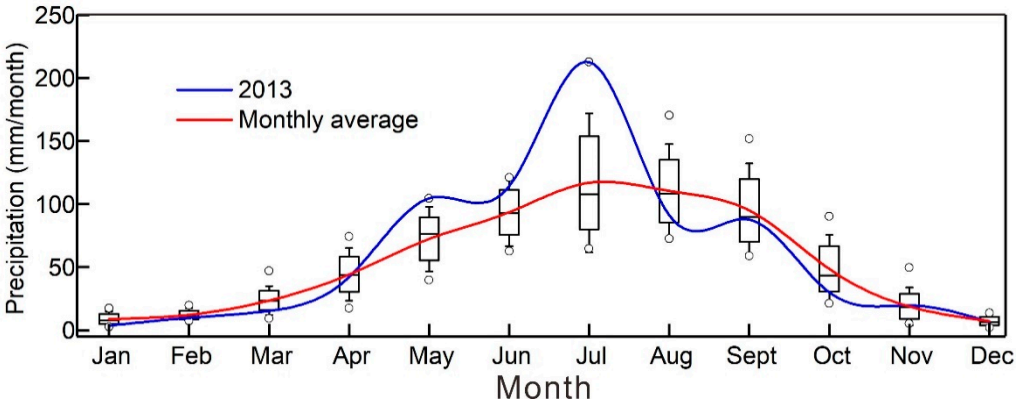

Figure 2. Map showing a comparison of the rainfall in each month in 2013 (blue line) with the average rainfall over the last 20 years from 2000 to 2020 (red line) in the Tianshui area.

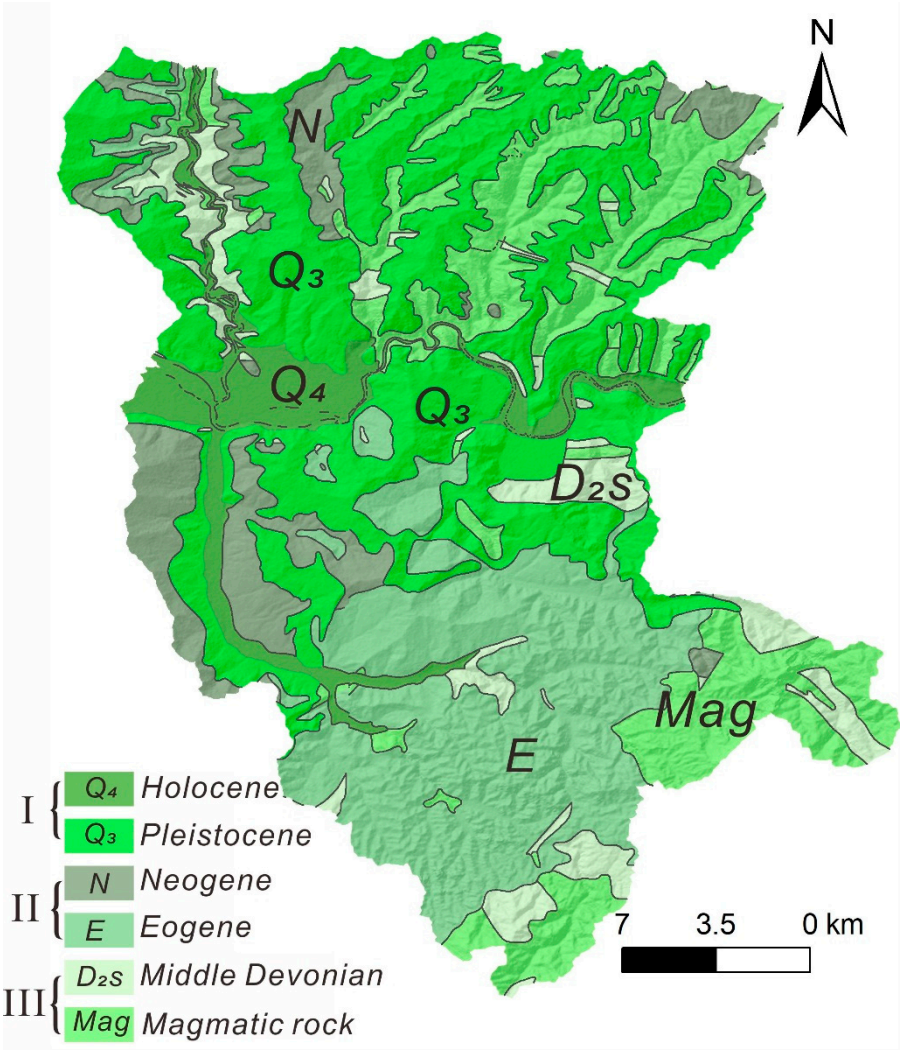

Figure 3. Geological map of the study area, obtained from 1:200,000 geological maps published by the China Geological Survey (http://dcc.cgs.gov.cn/);.

2.2. The Landslide Inventory

The landslide inventory used in this study area consisted of the landslides induced by the 2013 heavy rainfall event in the Tianshui area. The landslide inventory was visually interpreted by comparing the remote sensing images before and after the rainfall event, ensuring that the landslides interpreted were caused by the 2013 rainfall event [48]. The results showed that 14,982 landslides occurred within 500 km^2 of the entire study area, with a total landslide area of 20 km^2, and with the landslide number density and area density being 30/km^2 and 4%, respectively. The majority of these landslides were between 100 m^2 and 1000 m^2, accounting for about 70% of the total number (Figure 4c). The field investigations showed that most of the landslides were narrow and small-scale shallow loess landslides and loess mudflows. These shallow loess landslides frequently form in the upper valley, and some landslides are transformed into debris flows during the movement process [48,49].

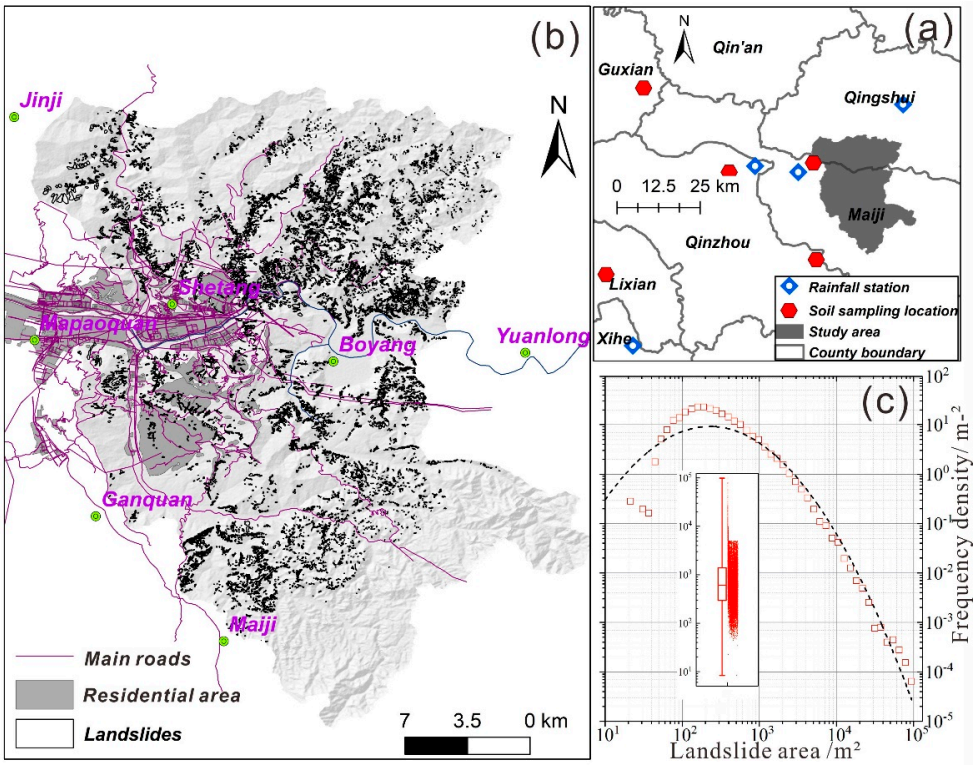

Figure 4. The distribution of residential areas, main roads, and landslides caused by the 2013 rainfall event in the study area: (**a**) The locations of the national rainfall stations and soil samples used in this study. (**b**) The distribution of rainfall-induced landslides of the 2013 rainfall event; (**c**) Frequency density of the landslide size (area in m^2) distribution. The road and resident data were obtained from the OpenStreetMap database (https://master.apis.dev.openstreetmap.org/export#map=11/35.2510/103.4308).

3. Data and Methods

3.1. Rainfall Data

Based on the China Meteorological Administration's rainfall stations, we gathered rainfall data every 12 h from June to July. To determine the geographical distribution of rainfall in the area, the most frequently used Kriging interpolation algorithm was employed to interpolate data from 14 national rainfall stations that were less than 100 km from the study area. According to the rainfall data from rainfall station 57,014 in the study area, the whole rainfall process lasted about 40 days—from June 19 to July 25—and the total accumulated rainfall in the study area was 470 mm, including four short-term heavy rainfall events (each short-term heavy rainfall event lasted about 2–3 days). The four heavy rain events took place from June 19 to 21, July 8 to 10, July 21 to 22, and July 24 to 25, respectively (Figure 5). In addition to these four rainfall events, there was also long-term intermittent rainfall.

Based on the rainfall station data and Kriging interpolation, we determined the spatial distribution of rainfall in different periods. Figure 6 shows the distribution of precipitation during the four heavy rainfall events. The results show that the spatial change in the cumulative rainfall was minor, with the precipitation in the north slightly higher than that in the south across the study area (Figure 6). Of the four short-term rainfall events, the rainfall of first event was the heaviest, at around 120~150 mm, accounting for 30% of all precipitation. The rainfall for the second event was estimated to be around 70–96 mm. Only two days separated the third and fourth rainfall events, which is a short time span; the cumulative precipitation of the two events was 100 and 37 mm, respectively.

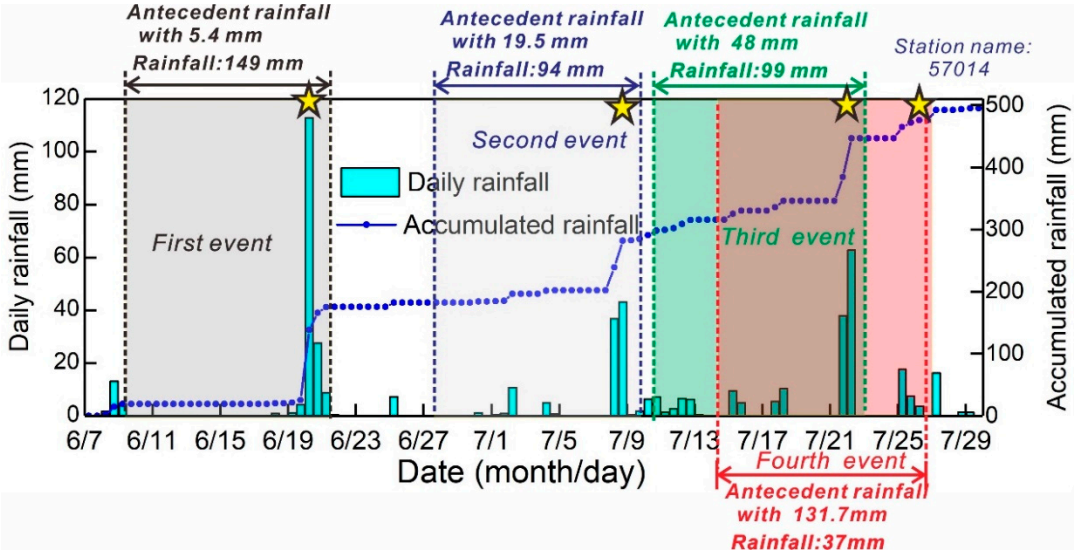

Figure 5. Rainfall data for every 12 h from June to July at rainfall station 57,014 in the study area.

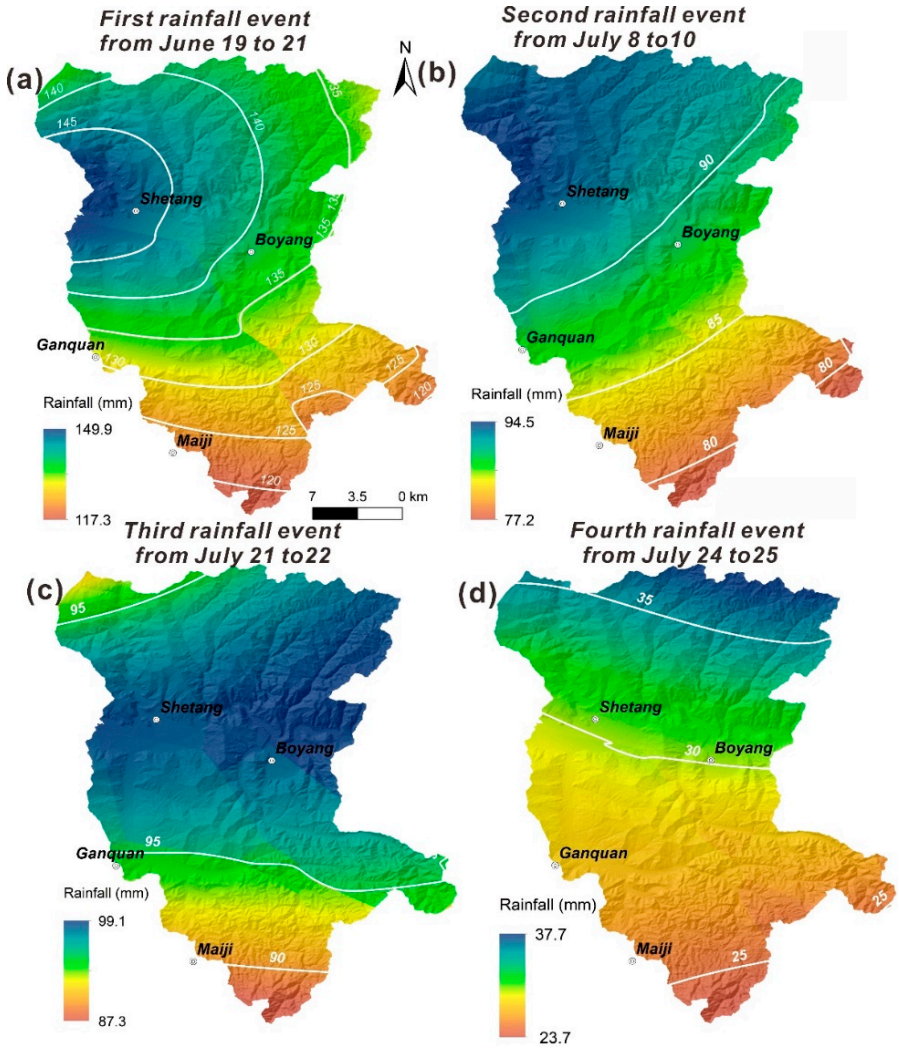

Figure 6. Spatial distribution of the rainfall with four events from June to July in the study area: (**a**) First rainfall event, from June 19 to 21. (**b**) Second rainfall event, from July 8 to 10. (**c**) Third rainfall event, from July 21 to 22. (**d**) Fourth rainfall event, from July 24 to 25.

3.2. Analysis of Soil Samples

The accuracy of the physical model is primarily determined by the input parameters, so accurate acquisition of soil parameters is critical for modeling prediction [31,32]. Based on previous studies, we collected information on the soil mechanical and hydrological parameters from 51 soil samples within a 50 km radius of the study area. Among the 51 soil samples, 47 were Quaternary soil samples and the remaining 4 were Tertiary mudstone samples (Figure 7). We analyzed the 47 Quaternary soil samples, and the results showed that, for the cohesion, the minimum value was 8 kPa, the maximum value was 37.2 kPa, and the average value was 22.4 kPa (Figure 7a). The internal friction angles ranged from 13.1° to 21°, with an average value of 18.0° (Figure 7b). The saturated hydraulic conductivity (Ks) ranged from a high of 250×10^{-6} cm/s to a low of 29×10^{-6} cm/s (Figure 7a). Simultaneously, we used quantile–quantile plots to determine whether these parameters conformed to the normal distribution. The results showed that the parameters of the Quaternary soil samples were in good agreement with the normal distribution (Figure 8). Additionally, we analyzed the four Tertiary mudstone samples (Figure 7b). The results showed that the samples had maximum and minimum cohesion of 25 kPa and 11 kPa, respectively, and maximum and minimum internal friction angles of 32 kPa and 22 kPa, respectively. The values of Ks were lower compared with the Quaternary soils, with a maximum and minimum of only 10^{-6} cm/s and 1×10^{-7} cm/s, respectively (Figure 7b). Given the small number of Tertiary samples, we assumed that the four Tertiary mudstone samples also followed the normal distribution.

To evaluate landslide threats in various scenarios and investigate the functional link between hillslope hydrology and slope materials, the topographical, soil hydrological, and mechanical features were mapped, as along with current land use. The slope angle of the research region was calculated based on the elevation data, which were generated using ALOS PALSAR DEM with 12.5 m resolution (Figure 9a). The China Geological Survey's 1:200,000 geological maps were used to obtain the lithology data (http://dcc.cgs.gov.cn/). The soil thickness distribution was evaluated using the Z-model developed by Saulnier et al. [50]. Based on previous studies [51,52], we assumed that the maximum value of the soil thickness in the study area was 6 m and the minimum was 0.5 m. Soil thickness can be estimated using Equation (1) (Figure 9b). Soil data were acquired from the Harmonized World Soil Database, which is a part of the World Soil Database established by the Food and Agriculture Organization of the United Nations (FAO) and the International Institute for Applied Systems Analysis (IIASA) (http://webarchive.iiasa.ac.at/Research/LUC/External-World-soil-database/HTML/). The soil types in the study area include loam and sandy clay loam, with loam primarily distributed in the north and middle of the study area and sandy clay loam primarily distributed in the south (Figure 9c). The land-use and land-cover (LULC) data were derived from the 10 m resolution global land-cover results [53] (Figure 9d). The parameter values used for different LULC were obtained from the USDA [54] (Table 1). Finally, the above input data were converted into a raster resolution of 12.5 m.

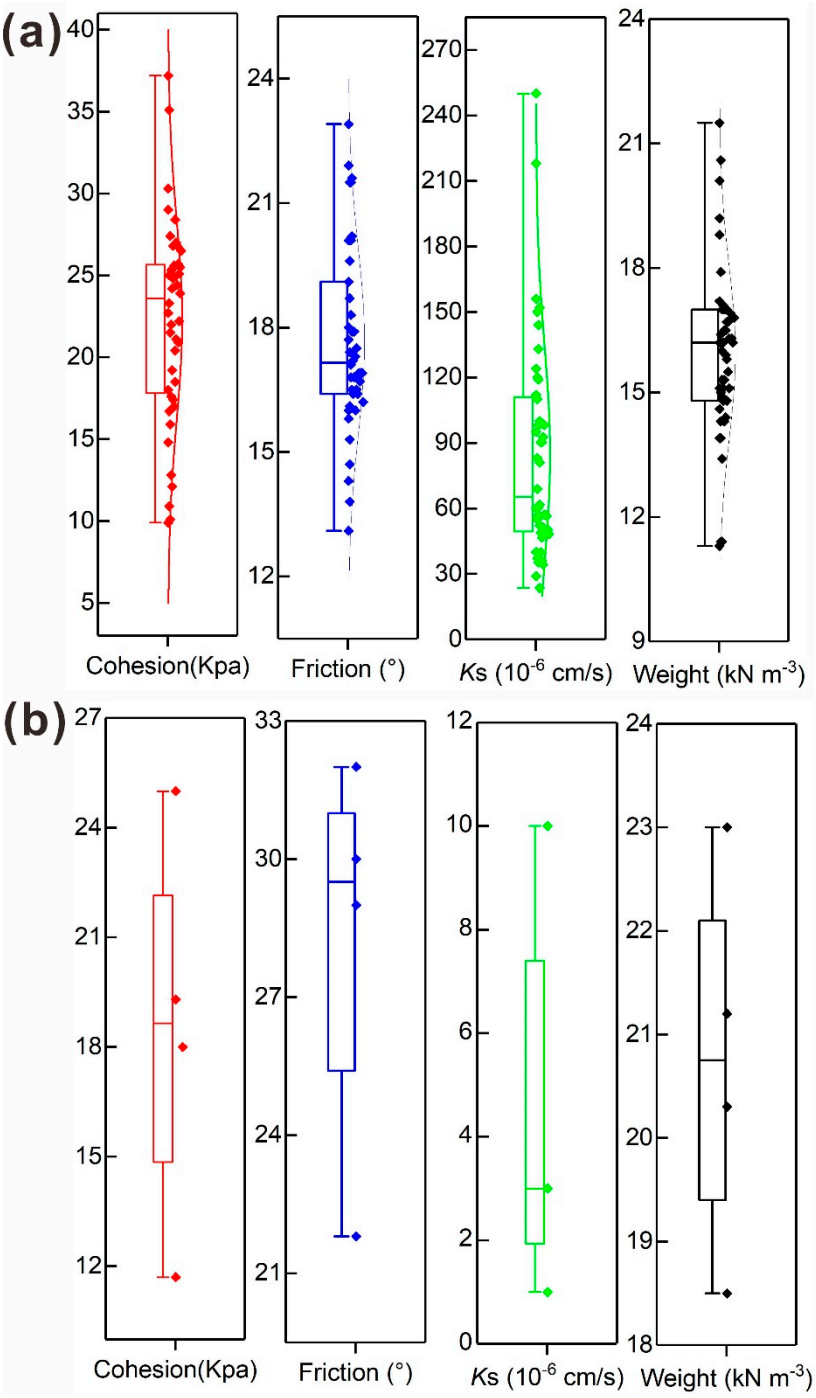

Figure 7. Distribution results of mechanical and hydrological parameters of (**a**) Quaternary soil samples and (**b**) Tertiary mudstone samples.

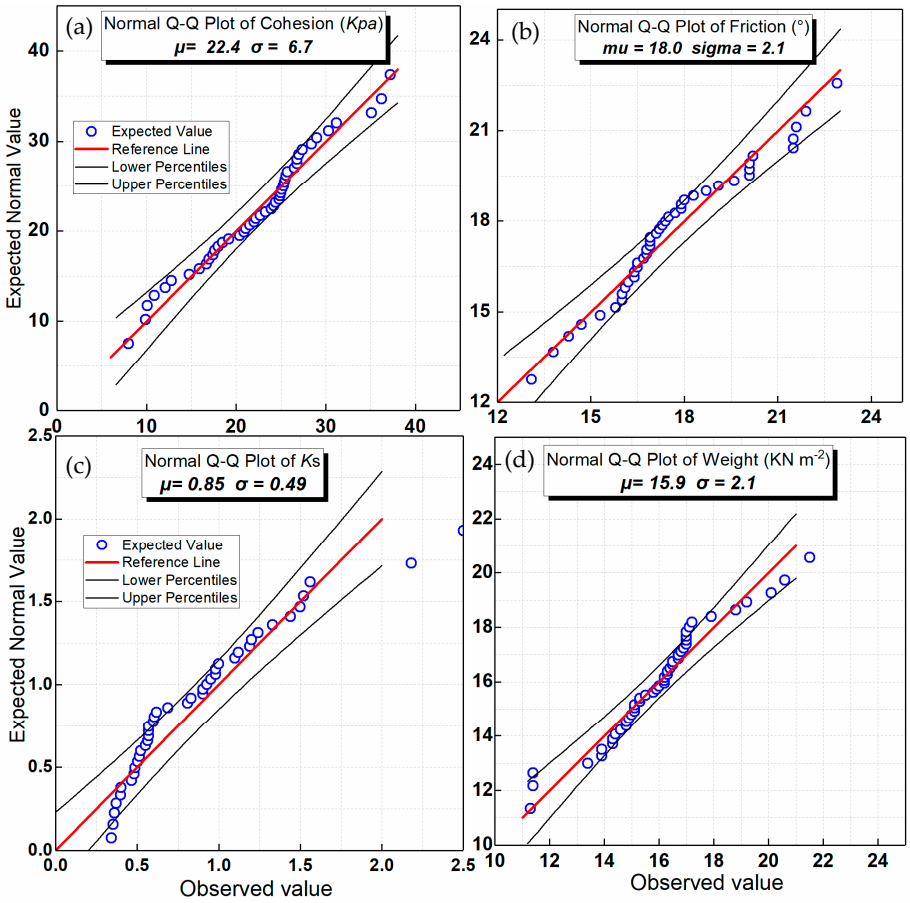

Figure 8. Quantile–quantile plots comparing the different input parameters to the normal distribution. The quantiles of each parameter are plotted against the quantiles of a standard normal distribution. The points will plot on a straight line if the two distributions are similar. (**a**) Cohesion. (**b**) Friction angle. (**c**) Saturated hydraulic conductivity (Ks). (**d**) Unit weight.

$$Z_i = Z_{max} - \left(\frac{h_i - h_{min}}{h_{max} - h_{min}}\right)(Z_{max} - Z_{min}) \quad (1)$$

where Z_{max} and Z_{min} are the maximum and minimum soil thicknesses, respectively, and h_{max} and h_{min} are the maximum and minimum elevations of the study area, respectively.

Table 1. The parameter values used for different LULC of the study area.

LULC	min (Kpa)	Crmax (Kpa)	CN-9	CN-10
Cropland (10)	2	4	69	79
Forest (20)	4	14	60	69
Grassland (30)	2	4	69	79
Shrubland (40)	3	6	65	76
Wetland (50)	0	0	100	100
Water (60)	0	0	100	100
Urban area (80)	0	1	92	96
Bare land(90)	0	0	100	100

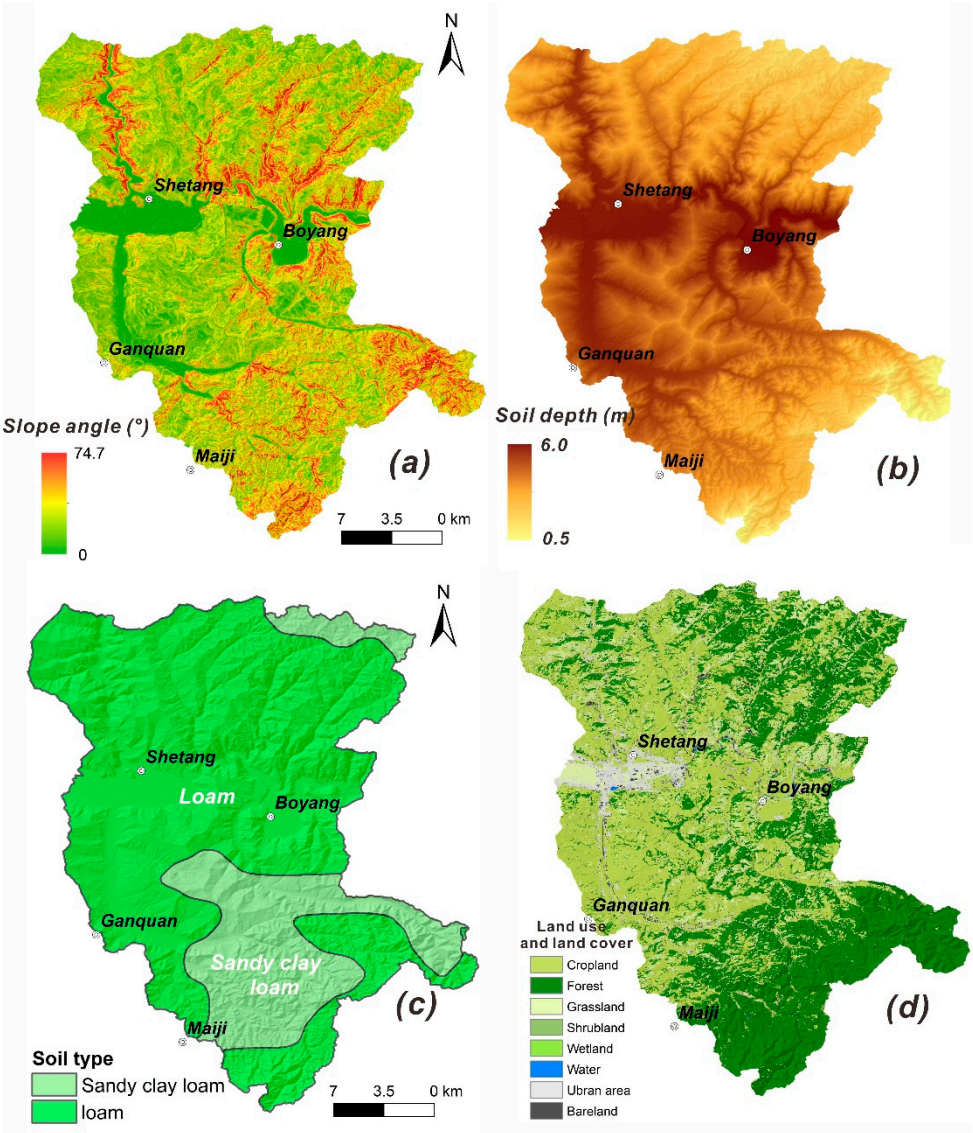

Figure 9. Map showing the input raster layers used for the FSLAM model: (**a**) Slope angle map. (**b**) Soil depth map. (**c**) Soil type map. (**d**) Land-use and land-cover (LULC) map.

CN-9 and CN-10 represent two different soil types in the study area: CN-9 represents sandy clay loam, and CN-10 represents loam.

3.3. Brief Description of the FSLAM Model

A physical-based model called the Fast Shallow Landslide Assessment Model (FSLAM) was created to estimate the likelihood of landslides occurring at the regional level [46,55]. Like other physical models, this one has two sub-models: (1) A geotechnical model that is used to calculate the slope stability using the popular infinite slope model, and (2) a hydrological model that determines the location of the water table as a result of rainfall infiltration into the soil layer. The following formula is used to calculate the factor of safety (FS):

$$FS = \frac{C}{g\rho_s z cos\theta sin\theta} + \left(1 - \frac{h}{z} \times \frac{\rho_w}{\rho_s}\right) \times \left(\frac{tan\varphi}{tan\theta}\right) \quad (2)$$

$$C = C_s + C_r \quad (3)$$

where C is the cohesion, ρ_s is the saturated soil density, ρ_w is the water density, θ is the slope angle, φ is the friction angle, h is the depth of the groundwater table, z is the depth of

the soil, C_s is the effective cohesion related to the lithology, and C_r is the apparent cohesion produced by the root strength.

The hydrological model considers the combined effects of medium- and long-term antecedent precipitation (P_a) and short-term event-specific precipitation (P_e) on the changes to the total groundwater table (h). The effect of the event-specific precipitation (Pe) applies vertical flow methods to compute the increase in the short-term water table (he), while the antecedent precipitation (Pa) determines the changes in the medium- and long-term groundwater levels (ha) using the lateral flow method. The final water table position (h) is determined as follows:

$$\mathrm{h} = h_a + h_e \tag{4}$$

During the mid–long-term, the P_a contributes to groundwater recharge (q_a) and, ultimately, determines the h_a at a steady state. The recharge is a reduced percentage of precipitation due to runoff and evapotranspiration, and it is also known as effective water infiltration into the soil layer. To properly quantify this recharge, the groundwater flow requires careful evaluation of the antecedent rainfall [56]. The FSLAM model employs the classic steady-state TOPMODEL to compute the antecedent effects of effective rainfall on groundwater levels [57], as applied in many models [58,59].

$$h_a = \left(\frac{a}{b}\right)\frac{q_a}{K_s sin\theta cos\theta}\left(\frac{\rho_w}{\rho_s}\right) \tag{5}$$

where a is the drainage area, b is the cell size, K_s is the saturated hydraulic conductivity, and q_a is the effective infiltration rate due to antecedent rainfall.

The FSLAM model uses the vertical flow approach to determine the rise in the water table (he), in contrast to the event-specific rainfall (Pe), which disregards the recharge contribution from upper areas (Figure 10). The FSLAM model considers the influence of rainfall events on the changes in groundwater levels due to vertical seepage from short-term heavy rainfall events. Several models have been calculated using the vertical infiltration method [60]. Vertical flow is concerned with the vadose zone, where unsaturated soil flow is represented by the Richards equation, which has complicated physics [17,61]. Models incorporating the Richards equation necessitate a large number of input parameters as well as extensive calibration. A computational difficulty is also presented by resolving these physics at the regional level. Such models are less applicable at the regional level due to their complexity and lengthy calculations, especially when numerous possibilities must be taken into account [46]. The FSLAM model, on the other hand, is intended to be fast at the regional scale, even with a high-resolution topography. As a result, rather than tracking the destabilization process, the FSLAM model examines the final value of the Fs. Given the soil porosity, total infiltration from a rainfall event is instantly translated into an increase in the water table:

$$h_e = q_e/n \tag{6}$$

where q_e represents the storm event infiltration, and n represents the soil porosity. To determine the value of q_e, the Pe is converted into groundwater recharge. The method selected in this study was the event-oriented SCS-CN model [54]. This model was created to compute the surface runoff associated with storm events, but it also computes the infiltration implicitly. The runoff curve number (also called a curve number, or simply CN) is an empirical parameter used in hydrology for predicting direct runoff or infiltration from excess rainfall. The model's success can be attributed to its simplicity, as it only requires one parameter. Finally, event infiltration q_e is computed by the SCS-CN model as follows:

$$q_e = P_e - \frac{(P_e - (5080/CN - 51))^2}{P_e + 4 \times (5080/CN - 51)} \tag{7}$$

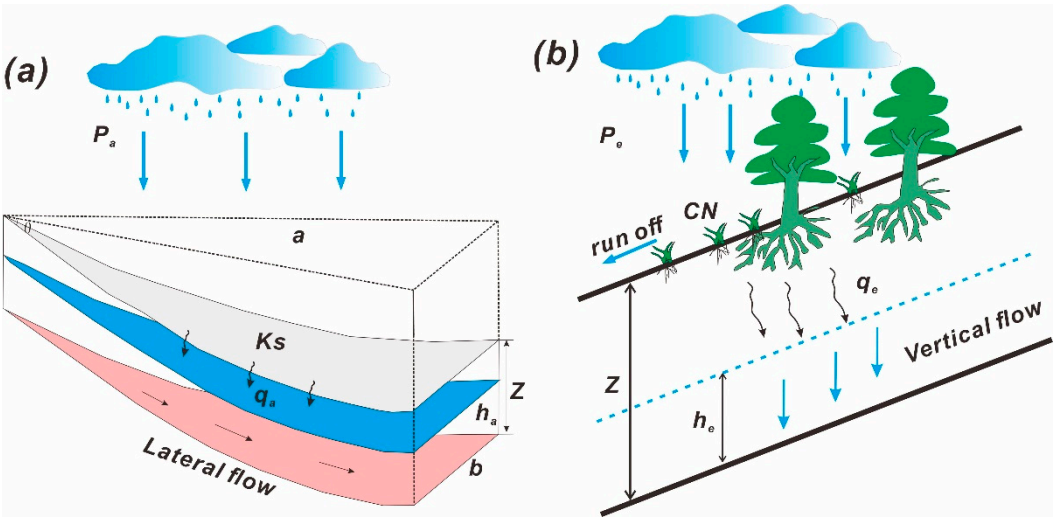

Figure 10. Hydrological models incorporated in FSLAM: (**a**) Incorporation of antecedent rainfall (Pa) by the lateral flow approach. (**b**) Incorporation of event-specific rainfall (Pe) by the vertical flow approach. The model graph is revised from the work of Medina, Hürlimann, Guo, Lloret, and Vaunat [46].

After combining all of the terms from the two different approaches to predicting rainfall, the final equation for the factor of safety (Fs) can be expressed as follows:

$$\mathrm{FS} = \frac{C}{g\rho_s z cos\theta sin\theta} + \left(1 - \left(\left(\left(\frac{a}{b}\right)\frac{q_a}{K_s sin\theta cos\theta}\left(\frac{\rho_w}{\rho_s}\right) + \frac{q_e}{n \times z}\right)\right) \times \frac{\rho_w}{\rho_s}\right) \times \left(\frac{tan\varphi}{tan\theta}\right) \quad (8)$$

Simultaneously, Monte Carlo simulation—a reliable and well-known method in applications concerning probability analyses and reliability studies—was used in this study to account for the uncertainty in soil properties [43,46,47]. We took into account the uncertainties of the two critical slope failure parameters: internal friction angle, and cohesion. Hence, when stochastic parameters are used, the model can calculate the probability of failure (PoF) of the study area.

4. Result

In this study, the short-term heavy rainfall event consisted of the precipitation from four events from June to July, and the antecedent precipitation was the total rainfall in the 10 days before a single heavy rainfall event (Figure 5). Based on the FSLAM model, we calculated the prediction results of the factor of safety (Fs) under four different heavy rainfall events in order to compare the impacts those heavy rainfall events on the triggering mechanisms of landslides. Figure 11 shows the distribution of the average values of 1000 predicted pictures. From Figure 11, we can observe that the trend of the Fs maps obtained from the four rainfall events is broadly similar. The majority of the areas with low Fs values are spread out on both sides of the gullies, which is relatively consistent with the actual landslide distribution. However, there are significant disparities in the predicted unstable area, i.e., the blue region where the Fs predicted for the four event rainfalls is less than 1. For the first rainfall event, there are few areas (blue areas) with Fs less than 1, and only sporadic areas show instability. When the second rainfall event is used as the input data, the unstable area (i.e., blue region) gradually increases, but the predicted failure area is still small compared to the actual landslide area, indicating that most landslides are still not predicted. However, when the third and fourth rainfall events are used as input data, the area with Fs less than 1 is expected to grow significantly. The majority of the blue areas are located near the gully area with a steep hillslope gradient, which corresponds to the spatial distribution of the actual landslides. Mainly, when the fourth rainfall event is used

as the input data, the majority of the actual landslides essentially occur in unstable areas (i.e., blue areas), indicating that most actual landslides are predicted.

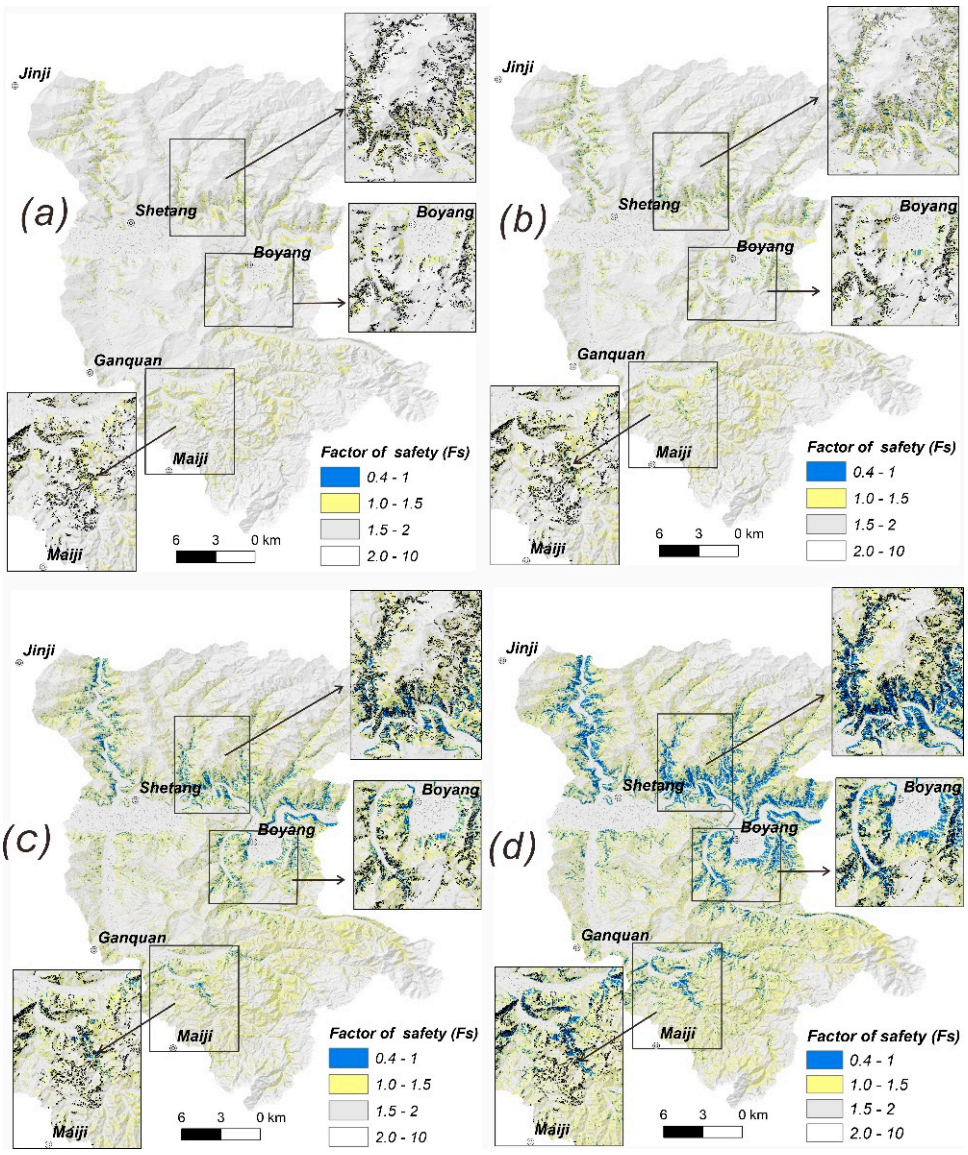

Figure 11. Prediction of the factor of safety (Fs) for shallow slope stability under four rainfall events: (**a**) First rainfall event, from June 19 to 21. (**b**) Second rainfall event, from July 8 to 10. (**c**) Third rainfall event, from July 21 to 22. (**d**) Fourth rainfall event, from July 24 to 25.

Figure 12 depicts the frequency density distribution of the factor of safety (Fs) under the four rainfall events. The results show that the Fs values of most areas are concentrated between 1 and 3, accounting for about 80% of the total area. We can also observe that the peak value of the frequency curve of the four rainfall events decreases. The peak values of Fs in the first and second rainfall events are 1.8 and 1.6, respectively, but the peaks associated with the third and fourth rainfall events are 1.3 and 1.1, respectively.

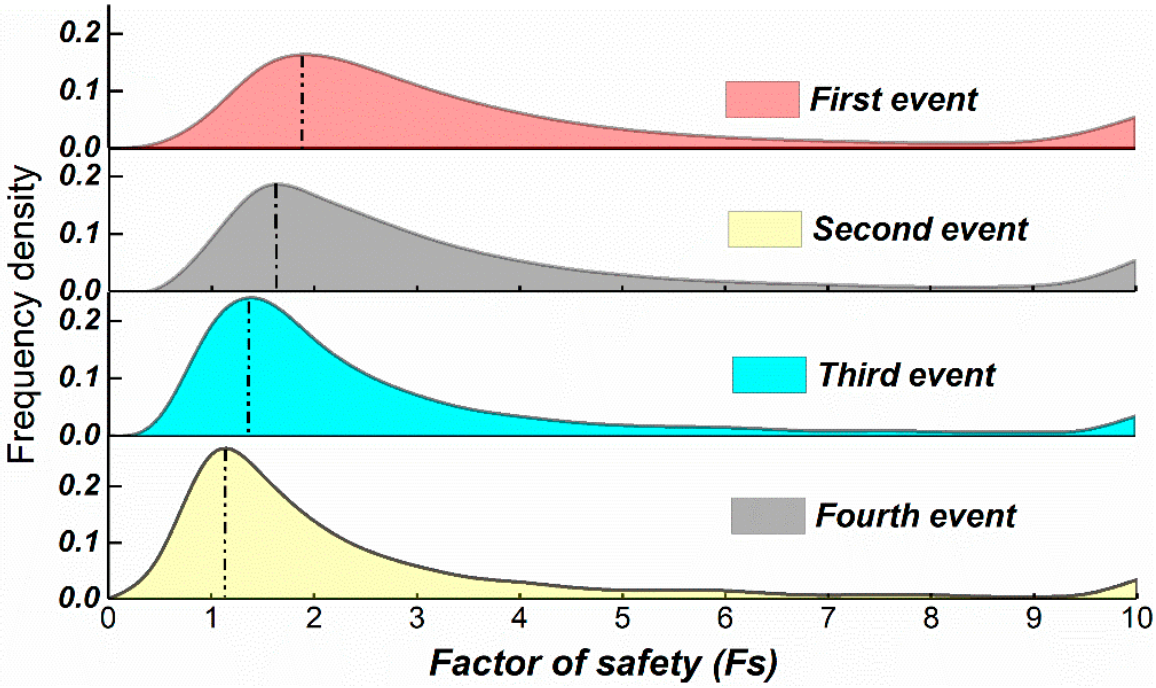

Figure 12. Frequency density distribution of the factor of safety (Fs) under four rainfall events.

The FSLAM model determined the slope failure probability (Pf) of the study area based on a Monte Carlo simulation of 1000 anticipated pictures of future landslides. The Pf value was classified into five groups based on a 0.25 interval: very low hazard (0.01), low hazard (0.01–0.25), moderate hazard (0.25–0.5), high hazard (0.5–0.75), and very high hazard (0.75–1). Figure 13 shows the prediction of Pf under the four rainfall events. The results show that the prediction results of Pf are roughly consistent with the actual landslide distribution. Simultaneously, for the first and second rainfall events, the majority of the landslides occur in the low-hazard area, with Pf of 0.01–0.25. For the third and fourth rainfall events, the predictions of high-hazard and very-high-hazard areas are significantly increased—especially for the fourth rainfall event, where the very-high-hazard areas (i.e., red areas) are increased considerably, and most of the landslides occur in the high-hazard and very-high-hazard areas.

To quantitatively analyze the hazard results, we counted the class area and the corresponding landslide areal density (LAD) of different hazard classes. Figure 14 shows the predicted hazard zoning results and the landslide number density (LND) distribution under the four rainfall events. The results show that nearly 90% of the study area is expected to consist of very-low- and low-hazard areas, with very-low-hazard areas accounting for around 80% and low-hazard areas accounting for roughly 10%. For very-high-hazard areas (i.e., red areas), the predicted areas of the third and fourth rainfall events account for 3% and 5% of the total area, respectively, while the predicted areas of the first two rainfall events account for less than 1%. In addition, from the LND curves in different hazard classes, we can observe that the LND of the third and fourth rainfall events increases with the hazard zoning, while the LND curves predicted by the first and second rainfall events do not show the same trend.

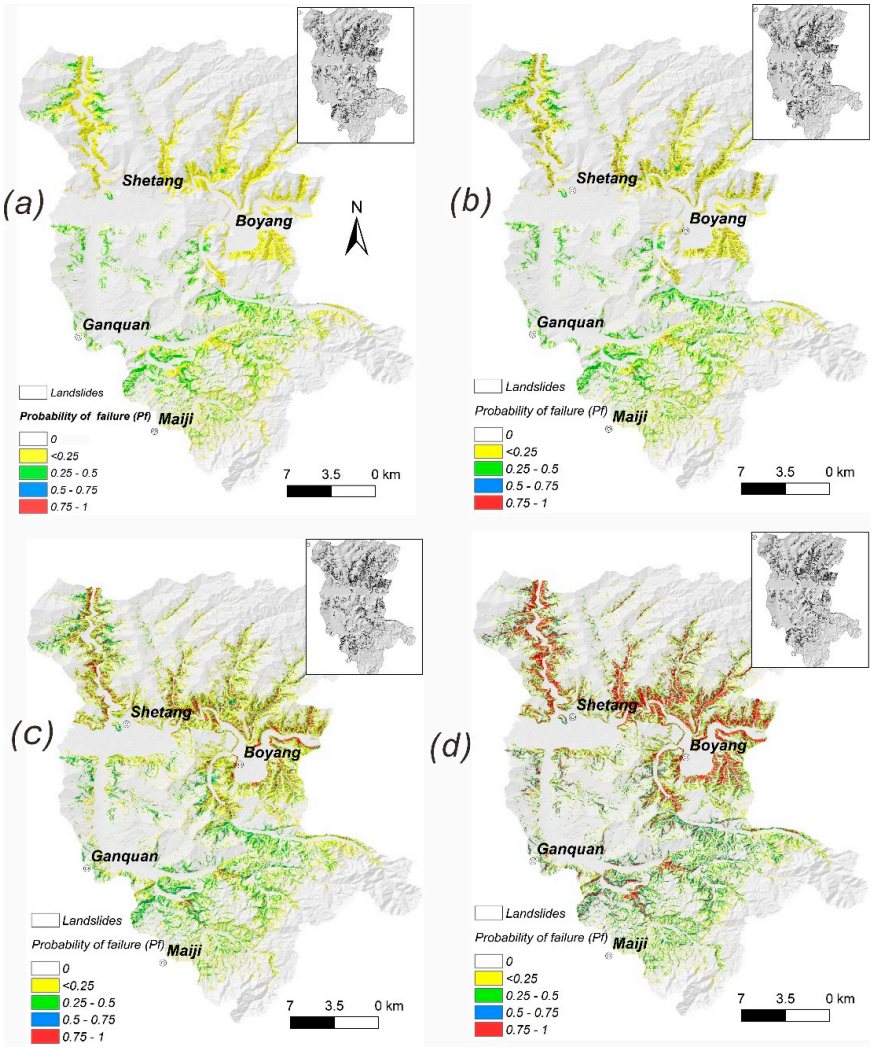

Figure 13. Prediction of probability of failure (Pf) under four rainfall events: (**a**) First rainfall event, from June 19 to 21. (**b**) Second rainfall event, from July 8 to 10. (**c**) Third rainfall event, from July 21 to 22. (**d**) Fourth rainfall event, from July 24 to 25.

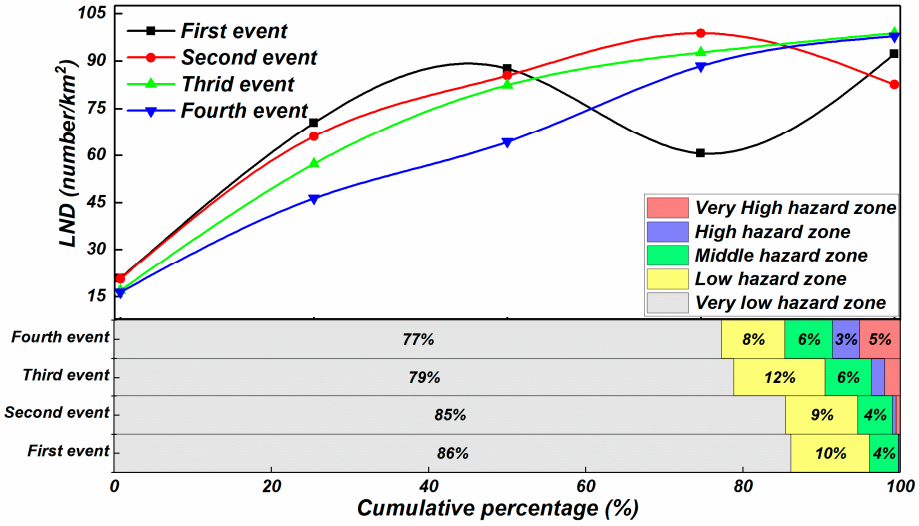

Figure 14. The predicted hazard zoning results and the landslide number density (LND) distribution under four rainfall events.

We used the actual landslide data to evaluate the prediction ability of the four hazard results. For this study, 14,982 landslides were used as sliding samples. We chose 15018 non-landslide samples at random from the landslide-free area, i.e., outside the buffer zone of landslide samples (buffer radius = 100 m). Finally, we used 30,000 samples to test the model performance calculated for the four rainfall events. Figure 15 presents the fourfold plots summarizing the numbers of samples correctly and incorrectly classified by the different prediction results [62,63]. The results show that the third and fourth rainfall events correctly predicted the location of most of the landslides, with about 2000 (true positives (TP), 14%) and 4300 landslides ((true positives)TP, 28%) correctly classified, respectively, while the other two rainfall events correctly predicted the fewest landslides. In addition, the accuracy of the four predicted hazard results was calculated. The accuracy is expressed as a percentage of correctly classified samples, which is expressed by accuracy = (TP + TN)/(TP + TN + FP + FN). The better the prediction ability, the higher the accuracy [62]. The results show that the accuracy of the four predicted results was 50.1%, 52.0%, 56.1%, and 63%, respectively, showing that the fourth rainfall event had the best prediction ability, while the third event had the second-best prediction ability.

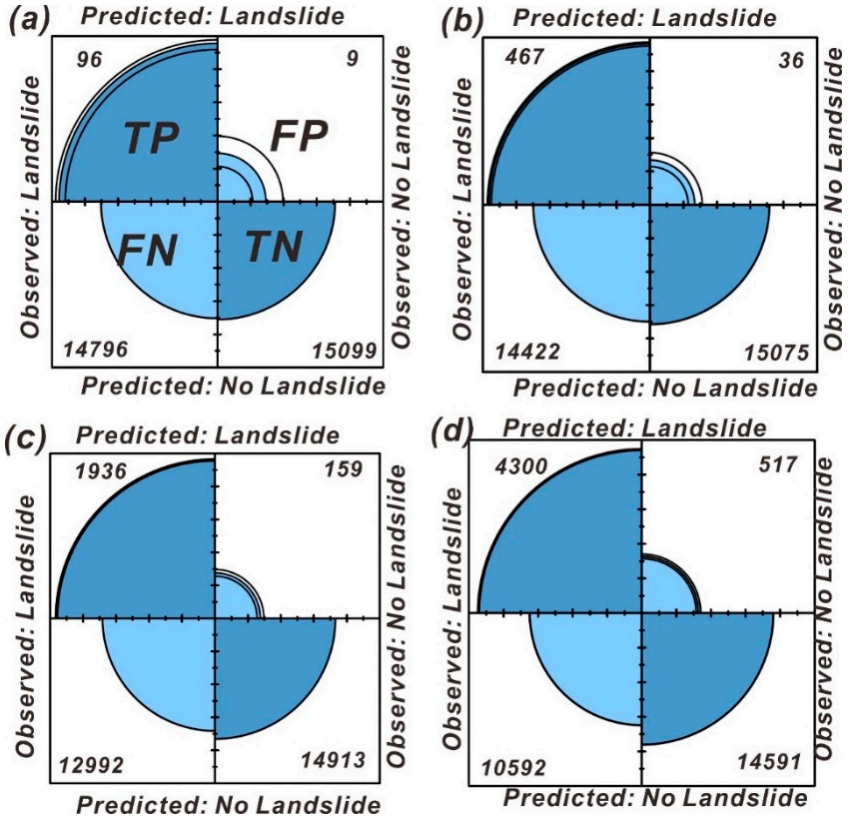

Figure 15. Fourfold plots summarizing the numbers of true positives (TP), true negatives (TN), false positives (FP), and false negatives (FN) for four rainfall events: (**a**) First event. (**b**) Second event. (**c**) Third event. (**d**) Fourth event.

To quantitatively evaluate the impact of the antecedent precipitation (P_a) on the predicted landslide area (P_{ls}), we calculated the predicted landslide area (P_{ls}) of four rainfall events with a Pf threshold of 0.5. Figure 16 shows the relationship between P_a and P_{ls} for the four rainfall events. From Figure 16, we can observe that the predicted landslide area (P_{ls}) is positively correlated with the antecedent precipitation (P_a). With the increase in P_a, the P_{ls} is also gradually increased. There is a solid linear link between the P_a and P_{ls} based on the fitting relationship of $P_{ls} = 0.3\ P_a - 0.26$, indicating that antecedent rainfall plays a major role in the occurrence of landslides in the region.

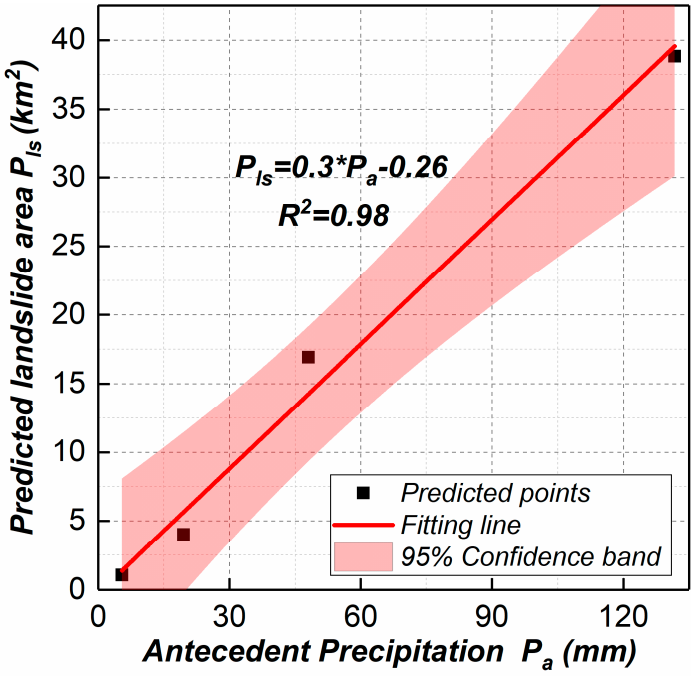

Figure 16. Relationship between antecedent precipitation (P_a) and the predicted landslide area (P_{ls}) for the four rainfall events.

5. Discussion

The occurrence of rainfall-induced landslides is a dynamic evolutionary process of rainfall events. For rainfall-induced landslides, the timing of landslide events frequently lags behind that of rainfall events. The two stages of rainfall that cause landslides are as follows: the first stage is the early stage, where the rainfall infiltration causes an increase in the water content and a gradual decline in the slope's shear strength of soil mass. The gradual deterioration of the slope structure creates the necessary conditions for the development of rainfall-induced landslides. The second stage is the key stage; the rainfall at this stage will directly lead to the occurrence of landslides. Thus, the development of the landslide is the result of the combined effects of antecedent rainfall and current rainfall events. However, most physical-based models only address either antecedent or current rainfall and do not account for both impacts on rainfall-induced landslides. Godt et al. [64] pointed out that rainfall with high intensity and short duration has a limited effect on the thickness of the triggered landslides. For the loess area, the rainfall infiltration depth of the loess is less than 1.5 m [65]; short-term heavy rainfall may only create a change in the water content of the shallow surface soil, with no impact on the deep groundwater level of the soil, and the antecedent rainfall is the main factor influencing changes in the deep groundwater levels.

Previous research found that the rains that cause the slope failure usually occur within 10 days of the landslide [66,67]. Therefore, in this study, the total rainfall within 10 days of each rainfall event was considered as the early effective rainfall. We evaluated the impact of four rainfall events on the occurrence of loess landslides using the FSLAM model. The results showed that the occurrence of loess landslides is more directly related to the antecedent rainfall. With the increase in P_a, the P_{ls} also gradually increased. There is a solid linear link between the P_a and P_{ls} based on the fitting relationship, indicating that antecedent rainfall plays a major role in the occurrence of landslides in the region (Figure 16).

At present, previous studies [49,68,69] have mainly considered the spatial distribution of this extreme-rainfall-induced mass landslide, and few studies have carried out the quantitative analysis of the rainfall processes and triggering mechanisms for landslide occurrence associated with this event. We used the FSLAM model to predict the spatial locations of landslides during the 2013 heavy rainfall event. The four rainfall events were

used as input data, and the results showed that the trend of the Fs maps obtained from the four rainfall events was essentially the same. The majority of the low-Fs areas were found on both sides of the gullies. However, there were significant disparities in the areas (blue areas) predicted for the four rainfall events as having Fs less than one, and the peak of the frequency density curve corresponding to the four events decreased, indicating that the four rainfall events had a different triggering ability on the rainfall-induced landslides (Figures 11 and 12). By comparing the predicted results of the four heavy rainfall events with the actual landslides, we can see that while the first and second heavy rainfall events produced the most precipitation of the four events, they did not predict many landslide areas. This may suggest that the first two rainfall processes were not the primary cause of slope failure, merely preparing for the landslides in the later period. The erosion and rainwater infiltration of the preceding rainfall had a strong impact on the slope body, and the instability area in the region rapidly increased on the basis of the first two heavy rainfall events, even though the third and fourth rainfall events were the smallest of the entire rainfall processes. Due to the hysteresis of rainfall-induced landslides, the formation of slope failures in the later period should be reflected in the promotion of the second heavy rainfall event, and the superposition of the fourth and third rainfall events ultimately determined the spatial distribution characteristics of the landslide induced by the 2013 heavy rainfall event.

6. Conclusions

In this study, in order to compare the impacts of four different heavy rainfall events on the likelihood of landslides, we conducted the physical-based spatiotemporal prediction of rainfall-induced landslides based on the FSLAM model. The model was validated using the actual landslide data of the 2013 rainfall event. The results show that the trend of the Fs maps obtained from the four rainfall events is the same. The majority of the areas with low Fs values are spread out on both sides of the gullies, which is relatively consistent with the actual landslide distribution. However, the areas where the predicted Fs was less than 1 (i.e., blue areas) have significant disparities, and the peak of the frequency density curve corresponding to the four events decreased, indicating that the four rainfall events had a different triggering ability on the rainfall-induced landslides. Additionally, we evaluated the impacts of the four rainfall events on the occurrence of loess landslides using the FSLAM model. The results showed that the occurrence of loess landslides is more directly related to the antecedent rainfall, and there was a solid linear link between the P_a and P_{ls} based on the fitting relationship of $P_{ls} = 0.3\ P_a - 0.26$. By comparing the distribution of the predicted results of the four heavy rainfall events with the actual landslides, we can conclude that the first two rainfall processes may not be the main reason for slope failure, serving only to prepare for the landslides in the later period. Finally, the superposition of the third and fourth rainfall events is the primary cause of the spatial distribution of rainfall-induced landslides. This study provides scientific support for understanding the spatiotemporal distribution and triggering mechanisms of rainstorm-type landslides, as well as the prediction and early warning of rainfall-induced landslides in the loess area.

Author Contributions: C.X. proposed the research concept and participated in data curation and analysis. S.M. designed the framework of this research, processed the relevant data, and wrote the manuscript. X.S. and Y.X. participated in data analysis and revised the manuscript. All authors have read and agreed to the published version of the manuscript.

Funding: This study was supported by the National Key Research and Development Program of China (2021YFB3901205).

Data Availability Statement: Not applicable.

Conflicts of Interest: The authors declare that they have no known competing financial interest.

References

1. Kirschbaum, D.; Kapnick, S.B.; Stanley, T.; Pascale, S. Changes in Extreme Precipitation and Landslides Over High Mountain Asia. *Geophys. Res. Lett.* **2020**, *47*, e2019GL085347. [CrossRef]
2. Emberson, R.; Kirschbaum, D.; Stanley, T. Global connections between El Nino and landslide impacts. *Nat. Commun.* **2021**, *12*, 2262. [CrossRef] [PubMed]
3. Petley, D. Global patterns of loss of life from landslides. *Geology* **2012**, *40*, 927–930. [CrossRef]
4. Lin, Q.; Wang, Y. Spatial and temporal analysis of a fatal landslide inventory in China from 1950 to 2016. *Landslides* **2018**, *15*, 2357–2372. [CrossRef]
5. Gariano, S.L.; Guzzetti, F. Landslides in a changing climate. *Earth-Sci. Rev.* **2016**, *162*, 227–252. [CrossRef]
6. Guo, Z.; Chen, L.; Yin, K.; Shrestha, D.P.; Zhang, L. Quantitative risk assessment of slow-moving landslides from the viewpoint of decision-making: A case study of the Three Gorges Reservoir in China. *Eng. Geol.* **2020**, *273*, 105667. [CrossRef]
7. Guzzetti, F.; Gariano, S.L.; Peruccacci, S.; Brunetti, M.T.; Marchesini, I.; Rossi, M.; Melillo, M. Geographical landslide early warning systems. *Earth-Sci. Rev.* **2020**, *200*, 102973. [CrossRef]
8. Baum, R.; Godt, J. Early warning of rainfall-induced shallow landslides and debris flows in the USA. *Landslides* **2010**, *7*, 259–272. [CrossRef]
9. Guzzetti, F.; Peruccacci, S.; Rossi, M.; Stark, C. The rainfall intensity-duration control of shallow landslides and debris flows: An update. *Landslides* **2008**, *5*, 3–17. [CrossRef]
10. Segoni, S.; Rosi, A.; Rossi, G.; Catani, F.; Casagli, N. Analysing the relationship between rainfalls and landslides to define a mosaic of triggering thresholds for regional scale warning systems. *Nat. Hazards Earth Syst. Sci.* **2014**, *2*, 2637–2648. [CrossRef]
11. Gioia, E.; Gabriella, S.; Ferretti, M.; Godt, J.; Baum, R.; Marincioni, F. Application of a process-based shallow landslide hazard model over a broad area in Central Italy. *Landslides* **2016**, *13*, 1197–1214. [CrossRef]
12. Park, H.J.; Lee, J.-H.; Woo, I. Assessment of rainfall-induced shallow landslide susceptibility using a GIS-based probabilistic approach. *Eng. Geol.* **2013**, *161*, 1–15. [CrossRef]
13. Xie, M.; Esaki, T.; Zhou, G. GIS-Based Probabilistic Mapping of Landslide Hazard Using a Three-Dimensional Deterministic Model. *Nat. Hazards* **2004**, *33*, 265–282. [CrossRef]
14. Pourghasemi, H.R.; Rahmati, O. Prediction of the landslide susceptibility: Which algorithm, which precision? *Catena* **2017**, *162*, 177–192. [CrossRef]
15. Bordoni, M.; Vivaldi, V.; Lucchelli, L.; Ciabatta, L.; Brocca, L.; Galve, J.; Meisina, C. Development of a data-driven model for spatial and temporal shallow landslide probability of occurrence at catchment scale. *Landslides* **2020**, *18*, 1209–1229. [CrossRef]
16. Tanyu, B.F.; Abbaspour, A.; Alimohammadlou, Y.; Tecuci, G. Landslide susceptibility analyses using Random Forest, C4.5, and C5.0 with balanced and unbalanced datasets. *Catena* **2021**, *203*, 105355. [CrossRef]
17. Baum, R.L.; Godt, J.W.; Savage, W.Z. Estimating the timing and location of shallow rainfall-induced landslides using a model for transient, unsaturated infiltration. *J. Geophys. Res. F Earth Surf.* **2010**, *115*, 126–153. [CrossRef]
18. Chae, B.-G.; Park, H.J.; Catani, F.; Simoni, A.; Berti, M. Landslide prediction, monitoring and early warning: A concise review of state-of-the-art. *Geosci. J.* **2017**, *21*, 1033–1070. [CrossRef]
19. Montgomery, D.R.; Dietrich, W.E.; Torres, R.; Anderson, S.P.; Heffner, J.T.; Loague, K. Hydrologic response of a steep, unchanneled valley to natural and applied rainfall. *Water Resour. Res.* **1997**, *33*, 91–109. [CrossRef]
20. Dietrich, W.E.; Reiss, R.; Hsu, M.-L.; Montgomery, D.R. A process-based model for colluvial soil depth and shallow landsliding using digital elevation data. *Hydrol. Process.* **1995**, *9*, 383–400. [CrossRef]
21. Pack, R.; Tarboton, D.; Goodwin, C.N. *SINMAP 2.0—A Stability Index Approach to Terrain Stability Hazard Mapping, User's Manual*; Utah State University: Logan, UT, USA, 1999.
22. Montrasio, L.; Valentino, R.; Losi, G.L. Rainfall-induced shallow landslides: A model for the triggering mechanism of some case studies in Northern Italy. *Landslides* **2009**, *6*, 241–251. [CrossRef]
23. Montrasio, L.; Valentino, R.; Corina, A.; Rossi, L.; Rudari, R. A prototype system for space–time assessment of rainfall-induced shallow landslides in Italy. *Nat. Hazards* **2014**, *74*, 1263–1290. [CrossRef]
24. Montrasio, L.; Valentino, R.; Meisina, C. Soil Saturation and Stability Analysis of a Test Site Slope Using the Shallow Landslide Instability Prediction (SLIP) Model. *Geotech. Geol. Eng.* **2018**, *36*, 2331–2342. [CrossRef]
25. An, H.; Viet, T.T.; Lee, G.; Kim, Y.; Kim, M.; Noh, S.; Noh, J. Development of time-variant landslide-prediction software considering three-dimensional subsurface unsaturated flow. *Environ. Model. Softw.* **2016**, *85*, 172–183. [CrossRef]
26. Tran, T.V.; Lee, G.; An, H.; Kim, M. Comparing the performance of TRIGRS and TiVaSS in spatial and temporal prediction of rainfall-induced shallow landslides. *Environ. Earth Sci.* **2017**, *76*, 315. [CrossRef]
27. Escobar-Wolf, R.; Sanders, J.D.; Vishnu, C.L.; Oommen, T.; Sajinkumar, K.S. A GIS Tool for Infinite Slope Stability Analysis (GIS-TISSA). *Geosci. Front.* **2021**, *12*, 756–768. [CrossRef]
28. He, X.; Hong, Y.; Vergara, H.; Zhang, K.; Kirstetter, P.-E.; Gourley, J.J.; Zhang, Y.; Qiao, G.; Liu, C. Development of a coupled hydrological-geotechnical framework for rainfall-induced landslides prediction. *J. Hydrol.* **2016**, *543*, 395–405. [CrossRef]
29. Zhang, K.; Xue, X.; Hong, Y.; Gourley, J.J.; Lu, N.; Wan, Z.; Hong, Z.; Wooten, R. iCRESTRIGRS: A coupled modeling system for cascading flood–landslide disaster forecasting. *Hydrol. Earth Syst. Sci.* **2016**, *20*, 5035–5048. [CrossRef]
30. Rossi, G.; Catani, F.; Leoni, L.; Segoni, S.; Tofani, V. HIRESSS: A physically based slope stability simulator for HPC applications. *Nat. Hazards Earth Syst. Sci.* **2013**, *13*, 151–166. [CrossRef]

31. Tofani, V.; Bicocchi, G.; Rossi, G.; Segoni, S.; D'Ambrosio, M.; Casagli, N.; Catani, F. Soil characterization for shallow landslides modeling: A case study in the Northern Apennines (Central Italy). *Landslides* **2017**, *14*, 755–770. [CrossRef]
32. Salvatici, T.; Tofani, V.; Rossi, G.; D'Ambrosio, M.; Tacconi Stefanelli, C.; Masi, E.B.; Rosi, A.; Pazzi, V.; Vannocci, P.; Petrolo, M.; et al. Application of a physically based model to forecast shallow landslides at a regional scale. *Nat. Hazards Earth Syst. Sci.* **2018**, *18*, 1919–1935. [CrossRef]
33. Canli, E.; Mergili, M.; Thiebes, B.; Glade, T. Probabilistic landslide ensemble prediction systems: Lessons to be learned from hydrology. *Nat. Hazards Earth Syst. Sci.* **2018**, *18*, 2183–2202. [CrossRef]
34. Cascini, L.; Ciurleo, M.; Di Nocera, S.; Gullà, G. A new–old approach for shallow landslide analysis and susceptibility zoning in fine-grained weathered soils of southern Italy. *Geomorphology* **2015**, *241*, 371–381. [CrossRef]
35. De Lima Neves Seefelder, C.; Koide, S.; Mergili, M. Does parameterization influence the performance of slope stability model results? A case study in Rio de Janeiro, Brazil. *Landslides* **2016**, *14*, 1389–1401. [CrossRef]
36. Schilirò, L.; Cevasco, A.; Esposito, C.; Mugnozza, G.S. Shallow landslide initiation on terraced slopes: Inferences from a physically based approach. *Geomat. Nat. Hazards Risk* **2018**, *9*, 295–324. [CrossRef]
37. Salciarini, D.; Godt, J.W.; Savage, W.Z.; Conversini, P.; Baum, R.L.; Michael, J.A. Modeling regional initiation of rainfall-induced shallow landslides in the eastern Umbria Region of central Italy. *Landslides* **2006**, *3*, 181–194. [CrossRef]
38. Raia, S.; Alvioli, M.; Rossi, M.; Baum, R.L.; Godt, J.; Guzzetti, F. Improving Predictive Power of Physically Based Rainfall-Induced Shallow Landslide Models: A Probabilistic Approach. *Geosci. Model Dev.* **2014**, *7*, 495. [CrossRef]
39. Lee, J.H.; Park, H.J. Assessment of shallow landslide susceptibility using the transient infiltration flow model and GIS-based probabilistic approach. *Landslides* **2015**, *13*, 885–903. [CrossRef]
40. Schilirò, L.; Esposito, C.; Scarascia Mugnozza, G. Evaluation of shallow landslide-triggering scenarios through a physically based approach: An example of application in the southern Messina area (northeastern Sicily, Italy). *Nat. Hazards Earth Syst. Sci.* **2015**, *15*, 2091–2109. [CrossRef]
41. Xue, C.; Nie, G.; Li, H.; Wang, J. Data assimilation with an improved particle filter and its application in the TRIGRS landslide model. *Nat. Hazards Earth Syst. Sci.* **2018**, *18*, 2801–2807. [CrossRef]
42. Park, H.J.; Jang, J.; Lee, J.-H. Assessment of rainfall-induced landslide susceptibility at the regional scale using a physically based model and fuzzy-based Monte Carlo simulation. *Landslides* **2019**, *16*, 695–713. [CrossRef]
43. Wu, S.-J.; Hsiao, Y.-H.; Yeh, K.-C.; Yang, S.-H. A probabilistic model for evaluating the reliability of rainfall thresholds for shallow landslides based on uncertainties in rainfall characteristics and soil properties. *Nat. Hazards* **2017**, *87*, 469–513. [CrossRef]
44. Salciarini, D.; Fanelli, G.; Tamagnini, C. A probabilistic model for rainfall—Induced shallow landslide prediction at the regional scale. *Landslides* **2017**, *14*, 1731–1746. [CrossRef]
45. Peres, D.J.; Cancelliere, A. Estimating return period of landslide triggering by Monte Carlo simulation. *J. Hydrol.* **2016**, *541*, 256–271. [CrossRef]
46. Medina, V.; Hürlimann, M.; Guo, Z.; Lloret, A.; Vaunat, J. Fast physically-based model for rainfall-induced landslide susceptibility assessment at regional scale. *Catena* **2021**, *201*, 105213. [CrossRef]
47. Hürlimann, M.; Guo, Z.; Puig-Polo, C.; Medina, V. Impacts of future climate and land cover changes on landslide susceptibility: Regional scale modelling in the Val d'Aran region (Pyrenees, Spain). *Landslides* **2022**, *19*, 99–118. [CrossRef]
48. Xu, Y.; Allen, M.B.; Zhang, W.; Li, W.; He, H. Landslide characteristics in the Loess Plateau, northern China. *Geomorphology* **2020**, *359*, 107150. [CrossRef]
49. Qi, T.; Zhao, Y.; Meng, X.; Chen, G.; Dijkstra, T. AI-Based Susceptibility Analysis of Shallow Landslides Induced by Heavy Rainfall in Tianshui, China. *Remote Sens.* **2021**, *13*, 1819. [CrossRef]
50. Saulnier, G.-M.; Beven, K.; Obled, C. Including spatially variable soil depths in TOPMODEL. *J. Hydrol.* **1997**, *202*, 158–172. [CrossRef]
51. He, J.; Qiu, H.; Qu, F.; Hu, S.; Yang, D.; Shen, Y.; Zhang, Y.; Sun, H.; Cao, M. Prediction of spatiotemporal stability and rainfall threshold of shallow landslides using the TRIGRS and Scoops3D models. *Catena* **2021**, *197*, 104999. [CrossRef]
52. Zhuang, J.; Peng, J.; Wang, G.; Iqbal, J.; Wang, Y.; Li, W.; Zhu, X. Prediction of rainfall-induced shallow landslides in the Loess Plateau, Yan'an, China, using the TRIGRS model. *Earth Surf. Process. Landf.* **2016**, *42*, 915–927. [CrossRef]
53. Gong, P.; Liu, H.; Zhang, M.; Li, C.; Wang, J.; Huang, H.; Clinton, N.; Ji, L.; Li, W.; Bai, Y.; et al. Stable classification with limited sample: Transferring a 30-m resolution sample set collected in 2015 to mapping 10-m resolution global land cover in 2017. *Sci. Bull.* **2019**, *64*, 370–373. [CrossRef] [PubMed]
54. USDA. *Urban Hydrology for Small Watersheds, 2nd ed*; Technical Release; USDA: Washington, DC, USA, 1986; Volume 55.
55. Guo, Z.; Torra, O.; Hürlimann, M.; Abancó, C.; Medina, V. FSLAM: A QGIS plugin for fast regional susceptibility assessment of rainfall-induced landslides. *Environ. Model. Softw.* **2022**, *150*, 105354. [CrossRef]
56. Papa, M.; Trentini, G.; Carbone, A.; Gallo, A. An integrated approach for debris flow hazard assessment—A case study on the Amalfi coast—Campania, Italy. *Ital. J. Eng. Geol. Environ.* **2011**, 983–992. [CrossRef]
57. Montgomery, D.R.; Dietrich, W.E. A physically based model for the topographic control on shallow landsliding. *Water Resour. Res.* **1994**, *30*, 1153–1171. [CrossRef]
58. Sarkar, S.; Roy, A.K.; Raha, P. Deterministic approach for susceptibility assessment of shallow debris slide in the Darjeeling Himalayas, India. *Catena* **2016**, *142*, 36–46. [CrossRef]

59. Bueechi, E.; Klimeš, J.; Frey, H.; Huggel, C.; Strozzi, T.; Cochachin, A. Regional-scale landslide susceptibility modelling in the Cordillera Blanca, Peru—A comparison of different approaches. *Landslides* **2018**, *16*, 395–407. [CrossRef]
60. Schiliro, L.; Montrasio, L.; Scarascia Mugnozza, G. Prediction of shallow landslide occurrence: Validation of a physically-based approach through a real case study. *Sci. Total. Environ.* **2016**, *569*, 134–144. [CrossRef]
61. Baum, R.L.; Savage, W.Z.; Godt, J.W. *TRIGRS—A Fortran Program for Transient Rainfall Infiltration and Grid-Based Regional Slope-Stability Analysis, Version 2.0*; US Geological Survey: Reston, VA, USA, 2008; p. 1159.
62. Rossi, M.; Guzzetti, F.; Reichenbach, P.; Mondini, A.C.; Peruccacci, S. Optimal landslide susceptibility zonation based on multiple forecasts. *Geomorphology* **2010**, *114*, 129–142. [CrossRef]
63. Jolliffe, I.T.; Stephenson, D.B. *Forecast Verification: A Practitioner's Guide in Atmospheric Science*; John Wiley & Sons: Hoboken, NJ, USA, 2003.
64. Godt, J.; Baum, R.L.; Savage, W.Z.; Salciarini, D.; Schulz, W.; Harp, E.L. Transient deterministic shallow landslide modeling: Requirements for susceptibility and hazard assessments in a GIS framework. *Eng. Geol.* **2008**, *102*, 214–226. [CrossRef]
65. Tong, X.; Peng, J.; Zhu, X.; Ma, P.; Meng, Z. Advantage infiltration depth of rainfall in loess area. *Bull. Soil Water Consevation* **2017**, *37*, 109–113.
66. Crozier, M.J. *Landslides: Causes, Consequences and Environment*; Croom Helm: London, UK, 1986; 245p.
67. Naidu, S.; Sajinkumar, K.S.; Oommen, T.; Anuja, V.J.; Samuel, R.; Muraleedharan, C. Early warning system for shallow landslides using rainfall threshold and slope stability analysis. *Geosci. Front.* **2017**, *9*, 1871–1882. [CrossRef]
68. Guo, F.; Meng, X.; Li, Z.; Xie, Z.; Chen, G.; He, Y. Characteristics and causes of assembled geohazards induced by the rainstorm on 25th July 2013 in Tianshui city, Gansu, China. *Moutain Res.* **2015**, *33*, 8.
69. Huang, S.; Cui, S.; Xin, P.; Wang, T.; Liang, C. Study on rainfall threshold and spatial distribution of clustered shallow landslides in Tianshui City on July 25. *J. Nat. Disasters* **2021**, *30*, 181–190.